Platinum-group elements, zircon Hf-O isotopes, and mineralogical constraints on magmatic evolution of the Pulang porphyry Cu-Au system, SW China

Cheng-Biao Leng [a,b,*], Jian-Feng Gao [a], Wei Terry Chen [a], Xing-Chun Zhang [a], Zhen-Dong Tian [a,c], Jian-Heng Guo [a,c]

[a] State Key Laboratory of Ore Deposit Geochemistry, Institute of Geochemistry, Chinese Academy of Sciences, Guiyang 550081, China
[b] Institute of Geology, Chinese Academy of Geological Sciences, Beijing 100037, China
[c] University of Chinese Academy of Sciences, Beijing 100049, China

ARTICLE INFO

ABSTRACT

A new model of porphyry Cu system, which involves pre-enrichment of Cu through sulfide accumulation near the mantle-crust boundary, has been recently proposed to account for variations of Cu endowment in different magmatic arcs. To test this model and explore the possible controlling factors of porphyry Cu metallogeny, we studied the mineralogy and platinum-group elements (PGE) geochemistry of the giant Pulang porphyry Cu-Au system in the Sanjiang Region, SW China. The Late Triassic Pulang intrusive complex comprises five phase of porphyritic stocks and dikes (ca. 217–212 Ma), which intruded a slightly older (ca. 230–218 Ma) volcanic-sedimentary sequence of the Tumugou Formation. Both the intrusive complex and the related volcanic wall rocks have similar PGE concentrations, Pd/Pt ratios and primitive mantle-normalized PGE patterns, indicating that no discernible sulfide cumulates were lost or gained during magmatic differentiation. The variation in PGE concentrations between different types of rocks at Pulang is probably ascribed to magma mixing between mafic and felsic end-members.

Two types of amphibole, i.e., high-Al (Al_2O_3 = 9.4–11.8 wt%) and low-Al (5.9–7.3 wt%) types, have been identified in the Pulang complex. It is estimated that the magma equilibrated with the high-Al amphibole may have contained up to 6.2 wt% H_2O, and was formed under 334–538 MPa (ca. 11–18 km deep eqv.) with oxygen fugacity (fO_2) between NNO + 0.2 and NNO + 1.5. In contrast, the magma that equilibrated with the low-Al amphibole was likely formed at a much shallower depth (89–202 MPa, ca. 3–7 km eqv.), and was more oxidized (NNO + 1.0–NNO + 1.7) with a low H_2O content (4.2–4.9 wt%). High fO_2 would increase sulfur solubility in the magma, thus prohibiting early removal of metals via sulfide precipitation. In addition, the higher H_2O content may have enhanced volatile exsolution from the evolving magmas at Pulang. We suggest that oxygen fugacity and H_2O content of the magma are two critical factors that controlled the Pulang porphyry Cu-Au metallogeny.

1. Introduction

Porphyry Cu (-Mo-Au) deposits are mainly formed in subduction-related magmatic arcs (e.g., Sillitoe, 1972, 2010; Richards, 2003), yet it is still unclear why some magmatic arcs (or sections of a magmatic arc) are more Cu-endowed (e.g., Andes; Sillitoe, 2012). It has been suggested that compressive arc settings, notably those led by aseismic ridge or flat-slab subduction, are favorable for producing large and high-grade porphyry Cu deposits (e.g., Sillitoe, 1998; Cooke et al., 2005; Tosdal et al., 2009). Some studies also argued that the reason for this heterogeneity of Cu endowment may lie deeper in the crust, e.g., a recent model proposed that high Cu endowment in some magmatic arcs may have led

by the accumulation of cupriferous sulfides at the base of continental arcs (e.g., Lee et al., 2012; Chiaradia, 2013; Hou et al., 2017). The model predicted that approximately 2/3 of the Cu budget of primary arc magmas is possibly stripped by sulfides near the lithospheric mantle-crust boundary. Consequently, large amounts of Cu-rich sulfides accumulated there may have been remobilized and contributed to later porphyry-related metallogenic event(s) (e.g., Hou et al., 2017). However, this hypothesis was challenged by Richards (2015), who argued that the volume of sulfide accumulations is too small to significantly affect the Cu budget of primary arc magmas. Sun et al. (2017) also suggested that such Cu pre-enrichment through sulfide saturation is not a prerequisite for generating large porphyry Cu deposits. Therefore, the importance of early accumulation of Cu-rich sulfides in later porphyry mineralization remains unclear.

Many recent studies, based largely on the platinum-group elements (PGE) geochemistry, were conducted to elucidate the sulfide saturation

* Corresponding author at: Institute of Geology, Chinese Academy of Geological Sciences, Beijing 100037, China.
E-mail address: lengchengbiao@vip.gyig.ac.cn (C.-B. Leng).

history in porphyry deposits (e.g., Gao et al., 2015; Park et al., 2015; Cocker et al., 2016; Hao et al., 2017). This is because PGE, as highly-chalcophile elements, have $D^{sulfide\ liquid/silicate\ melt}$ (partition coefficient between immiscible sulfide liquid and silicate melt) values at least two orders of magnitude above those of Cu and Au (e.g., Botcharnikov et al., 2011, 2013; Mungall and Brenan, 2014), making them a good indicator of sulfide saturation. Previous studies demonstrated that the timing and extent of sulfide accumulation exert an important influence on the tenor of the associated porphyry mineralization. For instance, Park et al. (2015) suggested that late sulfide saturation leads to at least two-fold enrichments of Cu and Au in the Niuatahi-Motutahi dacite (Tonga Rear Arc), and consequently controlled the Cu-Au mineralization. Meanwhile, a different sulfide saturation history is revealed at the El Abra porphyry Cu deposit (northern Chile; Cocker et al., 2016): Early removal of small amounts of sulfides may have resulted in PGE- and Au-depleted Cu mineralization at El Abra. Gao et al. (2015) suggested that early sulfide saturation may have removed most of the Cu and PGE from the magmas and inhibited important porphyry Cu mineralization at Tuwu. On the contrary, Economou-Eliopoulos and Eliopoulos (2000) reported high Pd and Pt contents (up to 490 ppb) in porphyry Cu deposits in Greece, which may have contributed by early sulfide accumulation during the magma emplacement. Thus, PGE geochemistry of porphyries can shed light on the timing and role of sulfide saturation in Cu mineralization.

In the Sanjiang Region, eastern margin of the Tibetan Plateau (SW China), a large number of porphyry Cu-Au deposits constitute an important mineralization belt (Fig. 1). The Pulang porphyry Cu-Au deposit, one of the largest deposits in the belt, is closely related to the Pulang

intrusive complex that intruded the upper Triassic clastic and volcanic rocks of the Tumugou Formation (Fig. 2). Previous studies suggested that the intrusive complex and the Tumugou Formation volcanic rocks were likely co-genetic and formed at different stages of the magmatic evolution (e.g., Wang et al., 2011; Leng et al., 2012), and thus these igneous rocks provide an excellent opportunity to evaluate the magmatic ore-forming processes. In this study, we present new zircon U-Pb age and Hf-O isotope data to clarify the temporal-genetic correlations between the porphyries and volcanic rocks. Mineralogical, whole-rock major/trace/PGE elements data for these rocks are also presented. We aim to 1) better understand the magmatic evolution of the Pulang porphyry system, (2) determine if there was early sulfide removal or accumulation in the lower crust, and if present (3) evaluate the degree of such accumulation, as well as (4) explore other potential favorable factors for the ore formation.

2. Geological background

2.1. Zhongdian region

A large number of porphyry Cu-Au deposits are distributed in the Zhongdian district (NW Yunnan), forming an important copper belt in the Sanjiang Region (Fig. 1b; Zeng et al., 2006; Hou et al., 2007; Li et al., 2011; Leng et al., 2012; Deng et al., 2014, 2017). Exposed stratigraphy in the district comprises mainly upper Triassic volcanic and sedimentary rocks (Fig. 1), including mafic to intermediate lavas, and intercalated fossiliferous limestone, clastic and pyroclastic rocks. These rocks were interpreted to have produced by the late Triassic west-
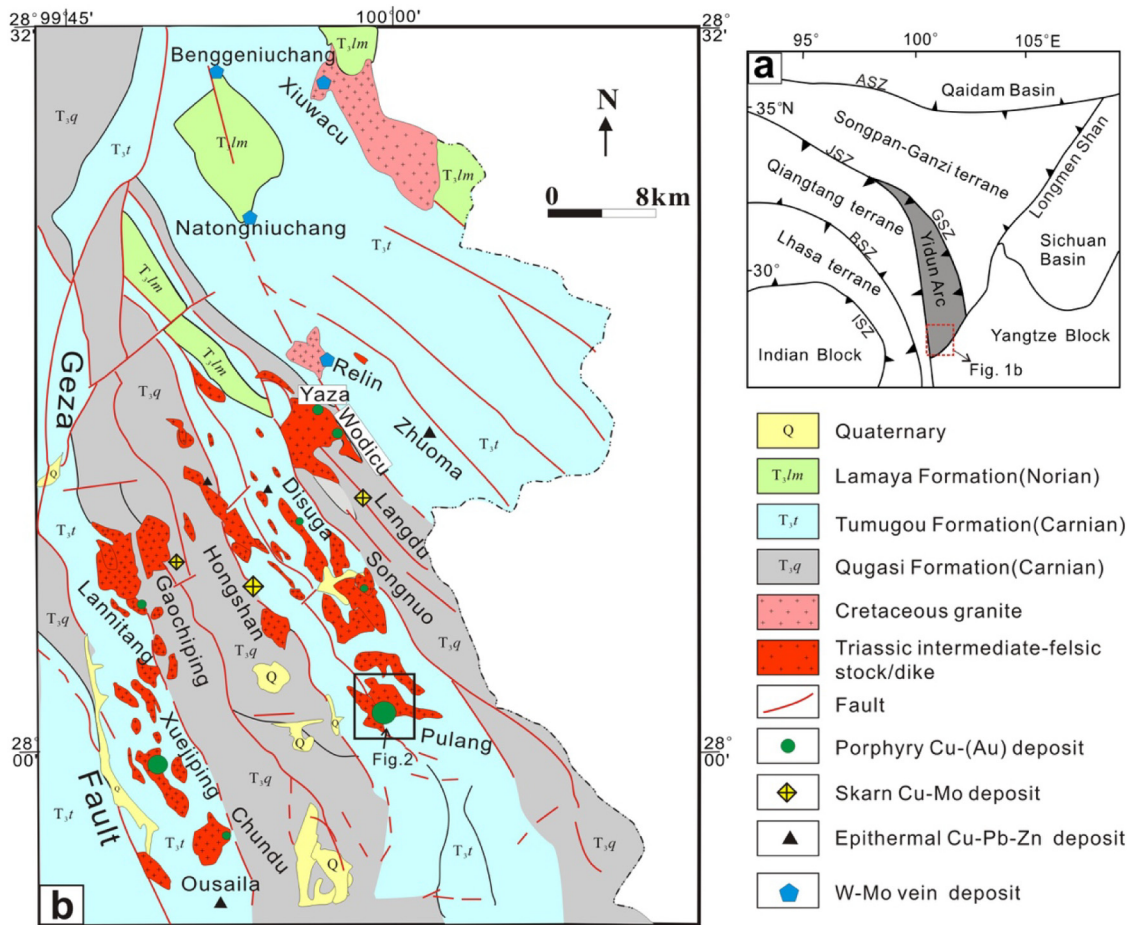
Fig. 1. (a) Tectonic framework of the Eastern Tibetan Plateau, highlighting the location of the study area (modified after Reid et al., 2005; Hou et al., 2007), and (b) simplified geological map of the Zhongdian district (modified after Leng et al., 2012). Abbreviation in a: ASZ = Ayimaqin-Kunlun suture zone; BSZ = Bangong-Nujiang suture zone; GSZ = Ganzi-Litang suture zone; ISZ = Indus-Yarlung suture zone; JSZ = Jinsha suture zone.
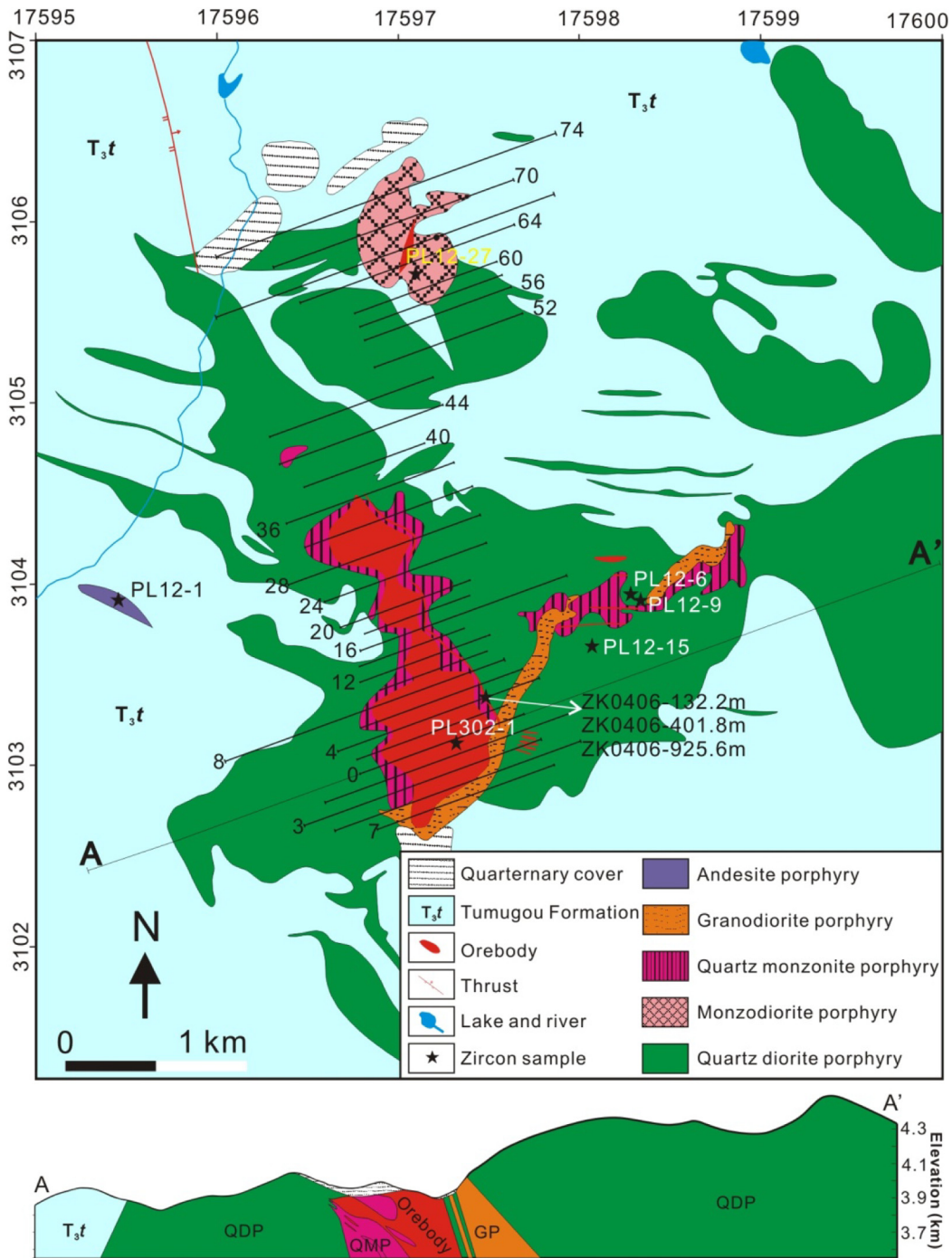
Fig. 2. Simplified geological map of the Pulang porphyry Cu-Au deposit (modified after Li et al., 2011), highlighting the sampling locations.

dipping subduction of the Ganzi-Litang ocean basin (e.g., Leng et al., 2012, 2014; Chen et al., 2014), followed by late Triassic to early Jurassic low-grade regional metamorphism (Reid et al., 2005). The mafic to intermediate lavas comprise trachyandesite with minor alkali basalt and dacite (Leng et al., 2014). These lavas were dated to be 230–218 Ma, and were suggested to be derived from partial melting of the lithospheric mantle that was metasomatised by subduction melts and/or fluids (e.g., Leng et al., 2012, 2014).

In the Zhongdian district, a large number of late Triassic felsic to intermediate stocks/dikes and the related porphyry and skarn deposits were emplaced into the volcanic-sedimentary sequence, probably along the NW-trending regional crustal-scale faults (Fig. 1b). These porphyritic stocks are andesitic to dacitic, and are composed of diorite,
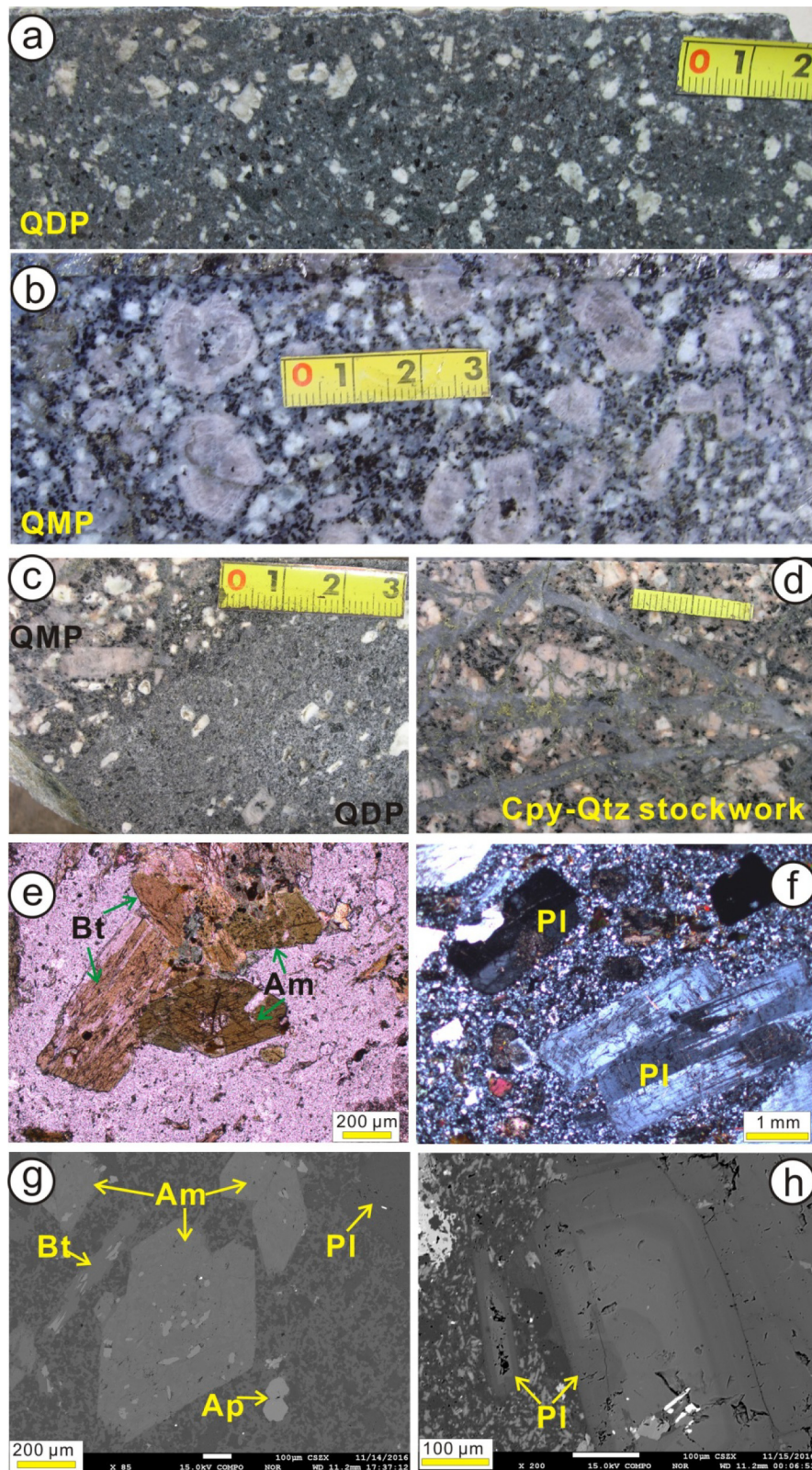
quartz diorite, quartz monzonite and granodiorite. There are also a few Mesozoic-Cenozoic W-Mo ore-bearing granitic batholiths in the district (Fig. 1b; Qu et al., 2002; X.S. Wang et al., 2014a), which were probably formed by the partial melting of Mesoproterozoic crustal materials in an intraplate extensional setting (X.S. Wang et al., 2014b).

2.2. Pulang Cu-Au deposit

Pulang is the largest porphyry deposit in the Zhongdian district, and contains proven reserves of ~4.31 million t (Mt) of Cu and 113 t of Au with an average grade of 0.34% and 0.09 g/t, respectively (Li et al., 2011). The deposit has been mined since 2017 under a designed annual production of ~50 kt Cu.

The Cu-Au mineralization is mainly hosted in the Pulang intrusive complex (16 km^2), which is composed of five porphyry stock/dike generations (Fig. 2) including (from oldest to youngest): pre-mineralized quartz diorite porphyry (QDP), syn-mineralized monzodiorite porphyry (MP) and quartz monzonite porphyry (QMP), and post-mineralized granodiorite porphyry (GP) and andesite porphyry (AP). The QDP is

Fig. 3. Photographs (a–d) and microphotographs (e–h) of some representative porphyries from the Pulang mine. (a) Quartz diorite porphyry (QDP, drill hole ZKE002, depth 3.5 m); (b) quartz monzonite porphyry (QMP, drill hole ZK0409, depth 996–997 m); (c) a gradational boundary between QDP and QMP stocks; (d) chalcopyrite-quartz stockwork veins in the QMP; (e) amphibole and biotite phenocrysts (QDP sample PLZK0416-821 m, plane polarized light), slightly altered; (f) plagioclase phenocrysts with Carlsbad twinning (QDP sample Pl12-32, cross polarized light); (g) amphibole and biotite phenocrysts locally replaced by actinolite and chlorite (QDP sample Pl12-8, BSE image); (h) normally-zoned plagioclase phenocrysts (QDP sample PLZK0416-821 m, BSE image). Abbreviations: Am = amphibole; Ap = apatite; Bt = biotite; Cpy = chalcopyrite; Kf = K-feldspar; Pl = plagioclase; Qtz = quartz.

fine- to medium-grained, and comprises plagioclase, hornblende, biotite, quartz, and minor K-feldspar phenocrysts in a microcrystalline groundmass (Fig. 3a, e, f). Phenocrysts are partially altered to actinolite, sericite, calcite and chlorite (Fig. 3e, g). The MP is fine-grained, and comprises plagioclase, K-feldspar, quartz, and minor biotite phenocrysts in a felsic groundmass, and experienced local chlorite and/or sericite alterations. The QMP is medium-grained, comprising K-feldspar, quartz and biotite phenocrysts in a felsic groundmass (Fig. 3b). The rocks have undergone potassic, phyllic and silicic alterations. These rocks are in gradational contact with QDP (Fig. 3c), indicating that the two rock types are largely coeval. GP (crosscutting the QDP and QMP stocks) has similar mineral assemblage to QDP, but is slightly altered. AP is mainly documented in drill cores, and crosscut all the above-mentioned porphyries. AP contains biotite, minor plagioclase and hornblende phenocrysts in an intermediate groundmass. Zircon, apatite, sphene, rutile and magnetite are common accessory minerals in the above-mentioned Pulang porphyries.

Many styles of hydrothermal alteration, including potassic, sericite, and propylitic, were extensively developed at Pulang (Zeng et al., 2006; Li et al., 2011). Alteration zonation is well developed in the deposit, with a potassic alteration core rimmed by propylitic alteration. Both alteration styles are locally overprinted by late sericite alteration. Veinlet, stockwork and/or disseminated Cu-Au ores are mainly hosted within the potassic core zone of the QMP stock, and are featured by an assemblage of chalcopyrite + pyrite ± molybdenite ± bornite (Fig. 3d). A molybdenite Re-Os age of 213 ± 3.8 Ma has been reported to constrain the timing of mineralization (Zeng et al., 2006). Several K-Ar and Ar-Ar plateau ages (216–210 Ma; Zeng et al., 2006; Wang, 2008; Li et al., 2011) were also obtained from the hydrothermal hornblende and biotite from the Pulang porphyries.

3. Analytical methods

3.1. Zircon U-Pb dating

Zircon grains were separated from the host rocks using conventional heavy liquid and magnetic separation techniques, and then hand-picked under a binocular microscope. Representative zircons were mounted in epoxy and then polished to about half their thickness for analysis. The zircons were observed using transmitted and reflected light microscopy and cathodoluminescence (CL) imaging to reveal their internal structures. Zircon U-Pb dating was performed on an Agilent 7500cs quadrupole ICPMS coupled with a 193 nm Coherent Ar-F gas laser at the University of Tasmania (Australia). Down-hole fractionation, instrument drift and mass bias correction factors for U-Pb ratios were calculated using two analyses of the primary standard 91500 (Wiedenbeck et al., 1995) and one analysis on each of the secondary standard zircons (Temora; Black et al., 2003; and GJ-1; Jackson et al., 2004) at the beginning of the session and every 15 zircon samples, using the same spot size and analytical conditions. The correction factor for the $^{207}Pb/^{206}Pb$ ratio was calculated using large spots of NIST610 analyzed every 30 unknowns and corrected using the values recommended by Baker et al. (2004). Each analysis on the zircon grains began with a 30 s blank gas measurement followed by a further 30 s of analysis with the laser on. Zircons were sampled using 32 μm spots using a frequency of 5 Hz and an energy density (measured at the sample surface) of approximately 2 J/cm². A flow of He carrier gas at a rate of 0.35 l/min carried particles ablated by the laser out of the chamber to be mixed with Ar gas and carried to the ICP-MS plasma torch. Isotopes measured were ^{49}Ti, ^{56}Fe, ^{90}Zr, ^{178}Hf, ^{202}Hg, ^{204}Pb, ^{206}Pb, ^{207}Pb, ^{208}Pb, ^{232}Th and ^{238}U with each element being measured every 0.16 s with longer counting time on the Pb isotopes compared to the other elements. Data was reduced using methods described in Meffre et al. (2008) and Sack et al. (2011). Element abundances on zircons were calculated using Zr as the internal standard element, assuming stoichiometric proportions (43.14% Zr in zircon) and using the NIST610 to correct for mass bias and drift. In addition, the titanium-in-zircon thermometry (Watson et al., 2006) is used to determine the zircon crystallization temperatures in the magmas.

3.2. In-situ zircon Hf-O isotopic analyses

Zircon oxygen isotopes were measured using the Cameca IMS-1280 SIMS at the Institute of Geology and Geophysics, Chinses Academy of Sciences. The detailed analytical procedures were described in Li et al. (2009). Cs^+ primary ion beam was used as the ion source, and the spot size is about 20 μm in diameter. Oxygen isotopes were measured using the multi-collection model on two off-axis Faraday cups. One analysis takes ~4 min. Uncertainties on individual analyses are usually better than 0.2‰ (1σ) (Li et al., 2010). The instrumental mass fractionation factor is corrected using the Penglai and Qinghu zircon standards with δ¹⁸O values of 5.31‰ ± 0.10‰ (2SD) and 5.4‰ ± 0.2‰ (2SD), respectively (Li et al., 2010, 2013).

Lu-Hf isotopes were analyzed on the same spots of the ion microprobe analysis, using a Neptune Plus MC-ICP-MS (Thermo Fisher Scientific) in combination with a Geolas 2005 excimer ArF laser ablation system (Lambda Physik) at the State Key Laboratory of Geological Processes and Mineral Resources, China University of Geosciences (Wuhan). All data were acquired on zircon in a single spot ablation mode at a spot size of 44 μm in this study. Detailed operating conditions of the laser ablation system and the MC-ICP-MS instrument and analytical method are the same as description by Hu et al. (2012). Off-line selection and integration of analytic signals, and mass bias calibrations were performed using ICPMSDataCal (Liu et al., 2010).

3.3. Whole-rock major, trace and platinum-group elements analyses

Major oxides of the samples were measured using X-ray fluorescence spectrometer (XRF) on fused glass beads at the ALS Chemex (Guangzhou) Co. Ltd. Trace elements were analyzed using ICP-MS at the State Key Laboratory of Ore Deposit Geochemistry (SKLODG), Institute of Geochemistry, Chinese Academy of Sciences, following the procedures of Qi et al. (2000). The analytical precision and accuracy for most major and trace elements measured are better than 5%.

PGE contents were determined using isotope dilution ICP-MS (ID-ICP-MS) at SKLODG, with a Carius tube technique (Qi et al., 2007, 2010). Approximately 10 g of sample powders was used in the analytical procedure. Ir, Ru, Pd, and Pt were measured with ID-ICP-MS and Rh was determined using ^{194}Pt as the internal standard (Qi et al., 2004). The analyses were monitored using a standard reference of WGB-1

Table 1
Summary of LA-ICP-MS zircon U-Pb dating results for the Pulang complex.

Sample ID	Lithology	$^{238}U/^{206}Pb$ age[a] (Ma)	±2 σ	T_{Ti}[b] (°C)	±σ
PL12-6	QDP	216.8	1.4	706	19
PL12-9		216.9	2.0	699	22
PL12-15		216.1	1.7	685	31
PL12-27	MP	215.9	1.3	695	20
PLZK0406-132.2 m	QMP	217.1	1.8	676	42
PLZK0406-401.8 m		216.0	1.2	682	27
PLZK0406-925.6 m		215.1	1.3	698	25
PL302-1	GP	214.2	1.7	731	21
PL12-1	AP	213.2	1.3	732	22
HN11-4[c]	TA	219.1	3.2	796	34

Abbreviation of lithology: AP = andesite porphyry, GP = granodiorite porphyry, MP = monzodiorite porphyry, QDP = quartz diorite porphyry, QMP = quartz monzonite porphyry, TA = trachyandesite.

[a] $^{238}U/^{206}Pb$ age was obtained by plots of $^{207}Pb/^{206}Pb$ vs. $^{238}U/^{206}Pb$ using the Isoplot package (Ludwig, 2012), except for PL12-15 which a weighted mean age is used (Fig. 4).

[b] T_{Ti} refers to titanium-in-zircon temperature of zircon, and is calculated based on the equation of $T_{Ti} = 4800 / (5.711 - Log\alpha_{SiO_2} + Log\alpha_{TiO_2} - LogTi) - 273$ (Watson et al., 2006), where α_{SiO_2} and α_{TiO_2} are assumed as 1.0 and 0.75, considering quartz and rutile exist in the rocks.

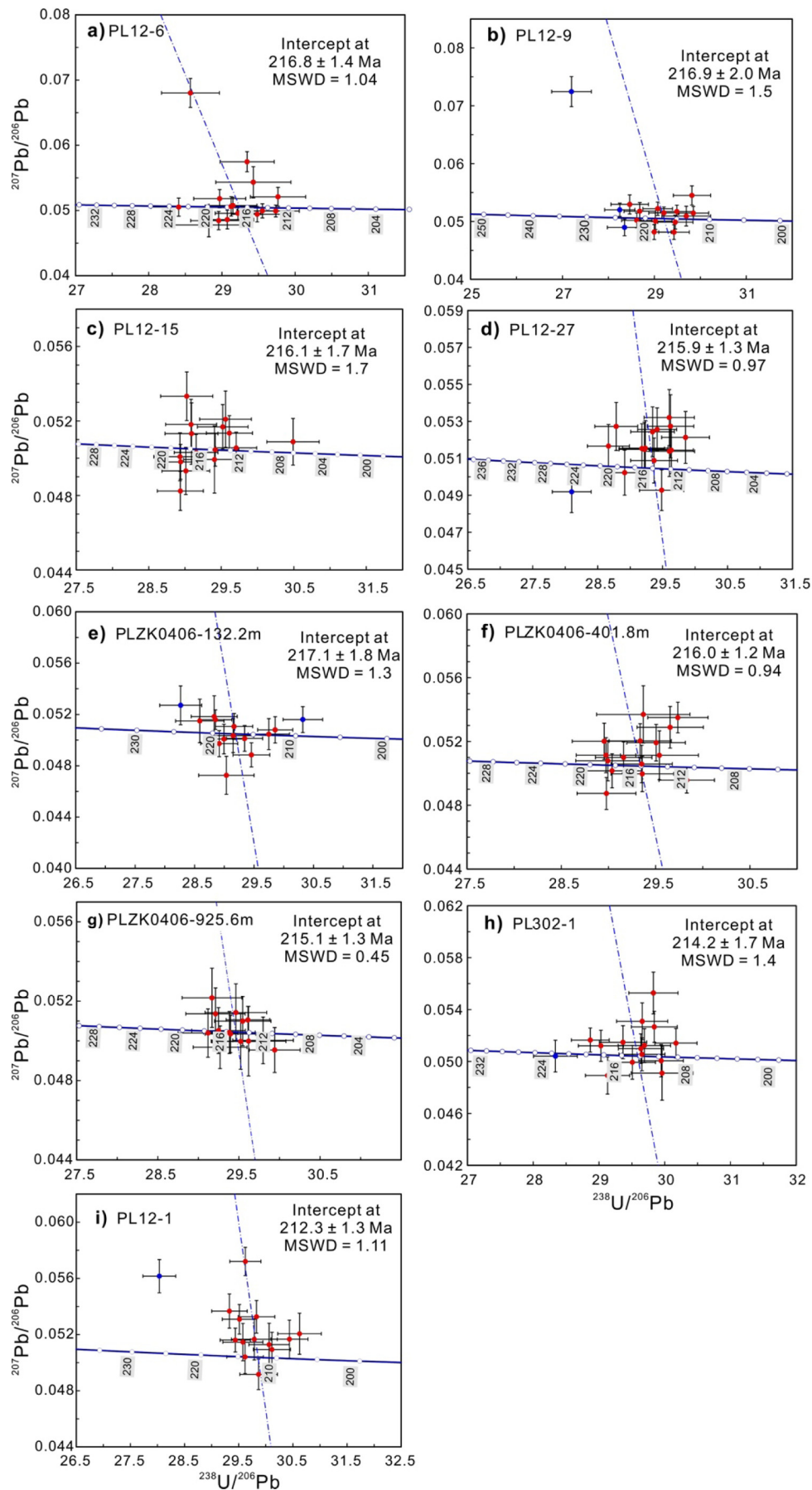[c] Data of HN11-4 from Leng et al. (2014) are shown for comparison.

Fig. 4. Terra-Wasserburg plots of the zircon U-Pb data for the Pulang complex. Blue spots are excluded in the age calculation.

(gabbro). The total procedural blanks were lower than 0.002 ppb for Ir, 0.003 ppb for Rh, 0.002 ppb for Ru, 0.012 ppb for Pd, and 0.020 ppb for Pt, respectively. The detection limits are 0.0016 ppb for Ir, 0.0015 ppb for Rh; 0.0014 ppb for Ru; 0.018 ppb for Pd; 0.011 ppb for Pt, respectively. Analytical precision is estimated to be better than 15% from the replication of standard materials.

3.4. EMPA mineral geochemical analysis

EMPA analysis of plagioclase and amphibole was undertaken using wavelength-dispersive X-rays analysis on a JEOL JXA-8100 electron microprobe at the Shandong Bureau Testing Center of China Metallurgical Geology Bureau (Jinan). The analyses were performed with a voltage of 15 keV and a sample beam of 20 nA focused on a spot of ~2 μm in diameter. Peak and background counting times were set at 20 and 10 s, respectively. The limits of detection are typically lower than 500 ppm, and analytical precision for major elements is better than 5%. In addition, The Probe-AMPH Excel spreadsheet (Tindle and Webb, 1994) was used to recalculate the amphibole compositions, and the Al-in-hornblende barometer of Johnson and Rutherford (1989) was used for pressure estimation. The methods of Ridolfi et al. (2010) were applied to calculate the temperature and oxygen fugacity (fO_2) of the magmas equilibrated with the amphibole.

4. Results

4.1. Zircon U-Pb age and titanium-in-zircon temperature

Nine porphyry samples (including 3 QDP, 3 QMP, 1 MP, 1 GP and 1 AP) were collected from the Pulang complex for the zircon U-Pb isotope analysis, and the whole dataset is presented in Supplemental Table 1 and summarized in Table 1. Most of zircon grains are colorless, transparent and euhedral, with clear concentric and oscillatory growth zoning under CL images. No inherited zircons or relict zircons cores were detected in this study.

Three nearly identical U-Pb ages (216.1 ± 1.7 to 216.9 ± 2.0 Ma) were obtained for the QDP samples (Table 1; Fig. 4a–c), representing the maximum age of the QDP stock emplacement. These samples have similar titanium-in-zircon temperatures (T_{Ti}) of 685 ± 31–706 ± 19 °C. Similarly, three QMP samples also have indistinguishable U-Pb ages (215.1 ± 1.3 to 217.1 ± 1.8 Ma; Fig. 4d–g) and consistent T_{Ti} temperatures (676 ± 42 to 698 ± 25 °C). In addition, one MP sample (PL12-27) yielded an age of 215.9 ± 1.3 Ma (Fig. 4h), and a T_{Ti} temperature of 695 ± 20 °C, broadly consistent with those of QDP and QMP. Zircons from the samples PL302-1 (GP) and PL12-1 (AP) are slightly younger (i.e., 214.2 ± 1.7 Ma, and 212.3 ± 1.3 Ma, respectively) (Table 1; Fig. 4i, j), but contain higher T_{Ti} temperatures (~730 °C) (Table 1; Fig. 5).

4.2. In-situ zircon Hf-O isotopes

Seven representative porphyry samples were collected from the Pulang complex for zircon Hf-O isotopes analyses. A trachyandesite sample (i.e. HN11-4) previously dated by Leng et al. (2014) was also analyzed for comparison. Twenty spots analyses were performed for each sample, and thus a total of 160 suites of zircon Hf-O isotope data were obtained (Supplemental Table 2).

In general, all the analyzed zircons from different samples have uniform $\delta^{18}O$ ratios (mean = 6.1 to 6.4‰) (Table 2, Fig. 6a–c). These zircons also have a limited $\varepsilon_{Hf}(t)$ range (-0.8 ± 0.3 to 0.1 ± 0.3) (Table 2, Fig. 6e–g). In contrast, the trachyandesite sample exhibits a slightly lower $\delta^{18}O$ value (5.8 ± 0.2‰; Fig. 6d) but a higher $\varepsilon_{Hf}(t)$ ratio (3.7 ± 0.3; Fig. 6h).
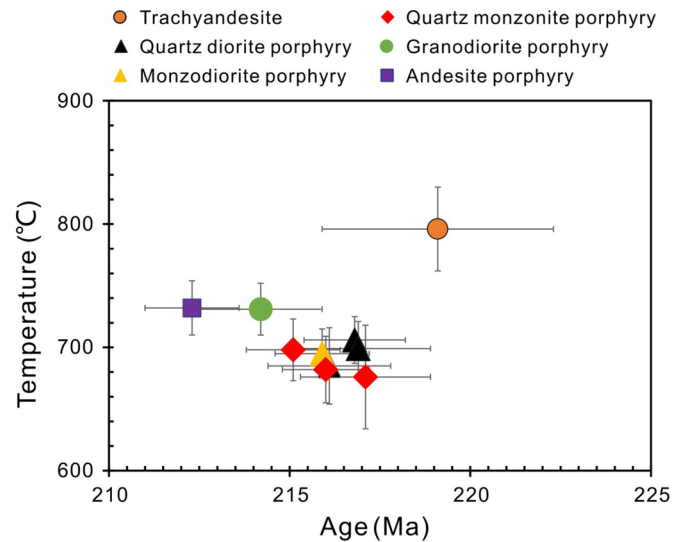

Fig. 5. Plot of U-Pb age vs. titanium-in-zircon temperature for zircons from the Pulang porphyries and volcanic wall rocks in the Zhongdian district.

4.3. Mineral chemistry

4.3.1. Plagioclase

Plagioclase is the dominant phenocryst type of the Pulang complex (Fig. 3a). Plagioclase phenocrysts are tabular, subhedral and 0.2 to 20 mm (mostly 1 to 10 mm) long. Most plagioclase phenocrysts are zoned (Fig. 3f), with CaO content gradually increasing from the crystal center to margin. The plagioclase compositions are highly variable (An_6 to An_{60}; Supplemental Table 3), but mostly around An_{30-50} (Fig. 7), similar to those of the plagioclase from the trachyandesite wall rocks (Leng et al., 2014).

4.3.2. Amphibole

Amphibole is another common phenocryst type for the Pulang QDP, GP and AP. Some course-grained amphibole phenocrysts (>0.1 mm) are locally replaced by actinolite and tremolite (Fig. 3e, g). All the analyzed grains belong to calcic amphiboles, and are mostly magnesiohornblende and minor tschermakite (Fig. 8). Based on the Al_2O_3 content, these amphiboles can be divided into high-Al ($Al_2O_3 = 9.4$–11.8 wt%) and low-Al ($Al_2O_3 = 5.9$–7.3 wt%) types (Fig. 9), although they are indistinguishable under BSE images (Fig. 3g). In general, the low-Al amphibole has lower TiO_2 and Na_2O concentrations than the high-Al type (Fig. 9; Supplemental Table 4).

4.4. Whole-rock elemental compositions

4.4.1. Major and trace elements

Thirty-five least-altered whole-rock samples from the Pulang complex have been analyzed (Supplemental Table 5). Compared to the

Table 2
Summary of zircon Hf-O isotopes of the Pulang porphyries and volcanic wall rocks.

Sample	Lithology	$\delta^{18}O$ (‰)		$\varepsilon_{Hf}(t)$	
		Range	Mean ± 2σ	Range	Mean ± 2σ
PL12-6	QDP	5.6–6.6	6.1 ± 0.1	−1.0–1.2	−0.4 ± 0.3
PL12-15		5.7–6.5	6.3 ± 0.1	−1.4–0.5	−0.6 ± 0.3
PLD0104		5.7–6.7	6.2 ± 0.1	−3.7–0.5	−0.3 ± 0.3
PL12-27	MP	5.9–6.9	6.1 ± 0.1	−0.9–0.8	0.0 ± 0.3
PL12-34	QMP	5.6–6.9	6.3 ± 0.1	−0.9–1.5	0.1 ± 0.3
PL302-1	GP	5.9–6.5	6.1 ± 0.1	−1.3–0.9	−0.3 ± 0.3
PL12-1	AP	6.0–6.8	6.4 ± 0.1	−2.1–1.0	−0.8 ± 0.3
HN11-4	TA	5.0–6.6	5.8 ± 0.2	1.9–6.2	3.7 ± 0.3

Note: abbreviations of lithology are as in Table 1.
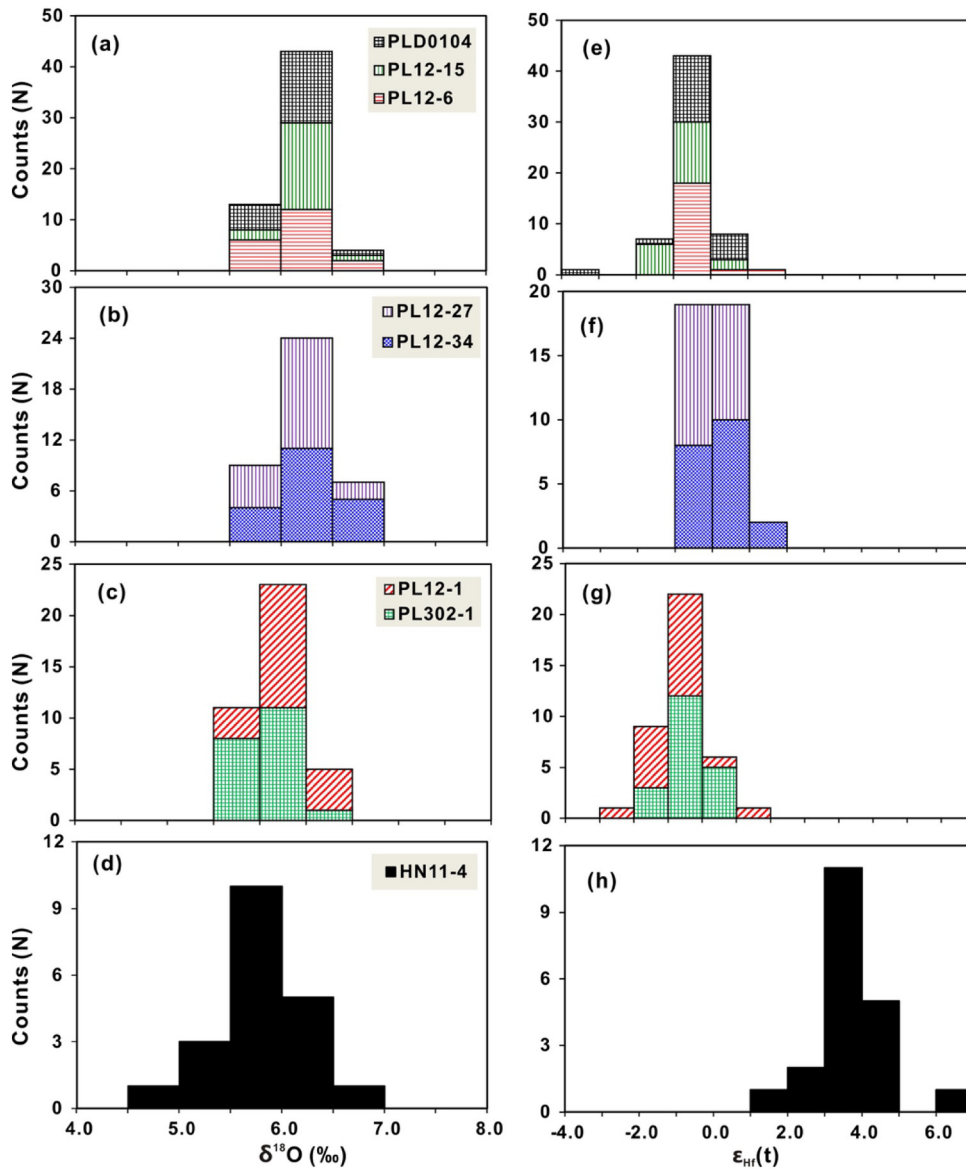
Fig. 6. Histogram of δ18O (a–d) and εHf(t) values (e–h) for the Pulang porphyries and volcanic wall rocks in the Zhongdian district.
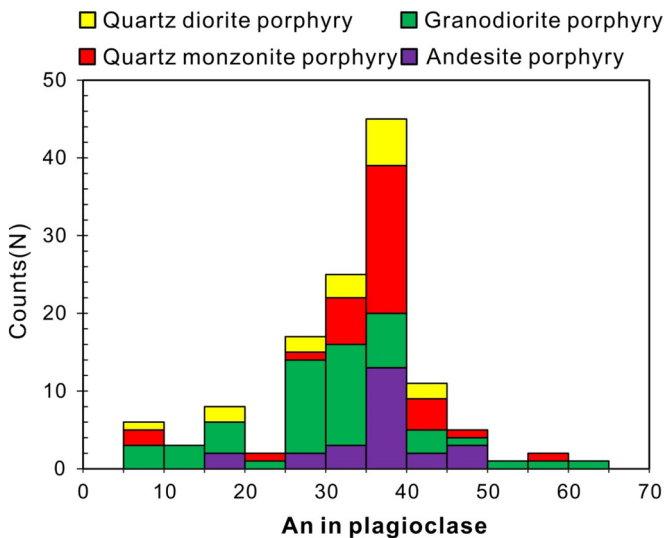

Fig. 7. Histogram of X_{An} of the plagioclase phenocrysts from the Pulang complex.
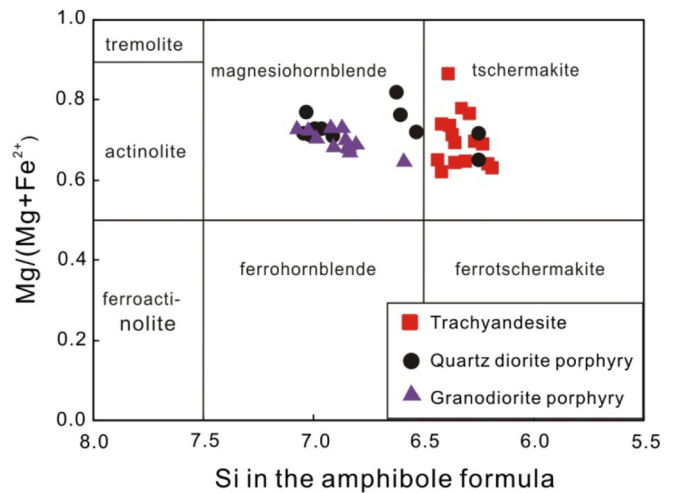

Fig. 8. Classification diagram of the amphiboles from the Pulang complex (after Leake et al., 1997). Data of the trachyandesite (Leng et al., 2014) are shown for comparison.
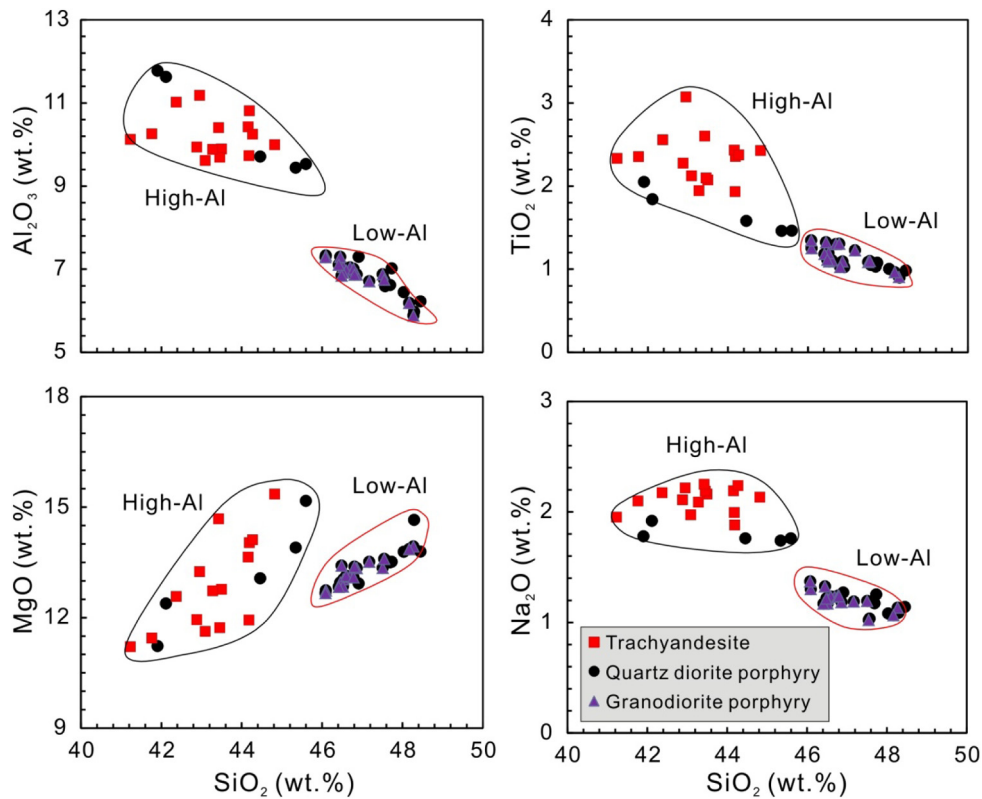
Fig. 9. Major elements variation diagram for the amphibole from the Pulang complex. Data of the trachyandesite (Leng et al., 2014) are shown for comparison.

volcanic wall rocks (e.g., Wang et al., 2011; Leng et al., 2014), these porphyries have a limited variation of SiO_2 (55.4 to 68.4 wt%), Al_2O_3 (12.4 to 16.2 wt%), MgO (1.7 to 4.9 wt%), Fe_2O_3 (2.4 to 8.3 wt%), CaO (1.02 to 5.38 wt%), and TiO_2 (0.46 to 1.06 wt%). These elements do not show clear correlations with SiO_2 in the Harker diagrams (Fig. 10a–f).

Although the trace element contents are highly variable in different rocks, their primitive mantle-normalized patterns are broadly subparallel (Fig. 11a). They are enriched in large ion lithophile elements (such as Rb, Ba, Sr, Th, and U), and depleted in Nb, Ta and Ti, resembling typical arc-type magmas (Tatsumi et al., 1986). Similarly, most samples show subparallel chondrite-normalized rare earth elements (REE) patterns (Fig. 11b). They are commonly characterized by strong enrichments of light REE (LREE), high $(La/Yb)_N$ ratios (15–35) and weak Eu anomalies (Fig. 11b).

4.4.2. Platinum-group elements

A total of twenty-four samples, including eight volcanic rock samples and 16 porphyry samples, were analyzed for their PGE and Au contents (Table 3). Duplicate analysis of a sample was conducted to reveal possible nugget effect.

The volcanic rocks contain 1.2–5.9 ppb of Pd (mean = 2.3 ± 1.5 ppb), 1.0–5.4 ppb of Pt (1.9 ± 1.4 ppb), and 0.1–0.8 ppb of Au (0.6 ± 0.3 ppb), with the Pd/Pt ratios of 1.0–1.6 (1.3 ± 0.3). Additionally, the sample DSG11-15 (alkaline basalt; Leng et al., 2014), one of the most mafic rocks in the study, contains the highest PGE contents (e.g., Pd = 5.9 ppb, and Pt = 5.4 ppb). Meanwhile, the porphyries exhibit a wide range of PGE concentrations, with those of Pd and Pt varying from 0.6 to 7.4 ppb (2.2 ± 1.7 ppb) and from 0.3 to 4.7 ppb (1.6 ± 1.1 ppb), respectively. Moreover, they contain much higher Au concentrations (mostly 1 to 20 ppb, up to 188 ppb) than the volcanic rocks, implying that Au is mobile and was probably added to the porphyries during the hydrothermal alteration at Pulang.

Overall, both volcanic and porphyritic rocks show similar primitive mantle-normalized PGE patterns (Fig. 12a, b). They are enriched in

Pd-group PGE (PPGE: Pt, Pd), and depleted in Ir-group PGE (IPGE: Ir, Ru), with Pt/Ir ratios of 22 to 452.

5. Discussion

5.1. Timing and duration of the Pulang intrusive activity

At Pulang, the pre-mineralized QDP has zircon U-Pb ages of ca. 216–217 Ma and titanium-in-zircon temperatures of 685–706 °C, indistinguishable from those of the syn-mineralized MP and QMP (215.9 Ma and 695 ± 20 °C, and 215.1–217.1 Ma and 676–698 °C, respectively) (Table 1; Fig. 5). The QMP has a gradational contact with the QDP, suggesting that the QDP and QMP (possibly also MP) were formed in a short timespan that cannot be distinguished by LA-ICP-MS dating method. They are slightly older than the potassic alteration and the related mineralization (ca. 213–210 Ma) (Zeng et al., 2006; Wang, 2008; Li et al., 2011). The post-mineralized GP and AP dikes are slightly younger (214 Ma and 212 Ma, respectively) (Table 1). Zircons from these two slightly younger dikes yielded an elevated titanium-in-zircon temperature (~730 °C; Fig. 5), indicating that the late dike emplacements were likely triggered by brief injection of hotter magmas, which promoted the incremental growth of the Pulang complex.

In summary, the duration of the Pulang complex may last only several millions of years, rather than tens of million years as previously considered (e.g., Zeng et al., 2006; Pang et al., 2009).

5.2. Genetic link between porphyries and volcanic rocks at Pulang

Porphyry stocks, as by-products of subduction-related magmas, are commonly emplaced in a subvolcanic environment covered by a volcanic edifice of pyroclastic rocks and/or lava flows (e.g., Sillitoe, 1973, 2010), which is also documented at Pulang. However, the genetic link between the intrusive and extrusive rocks is not always clear. Three models have been proposed to interpret this linkage: (1) fractional
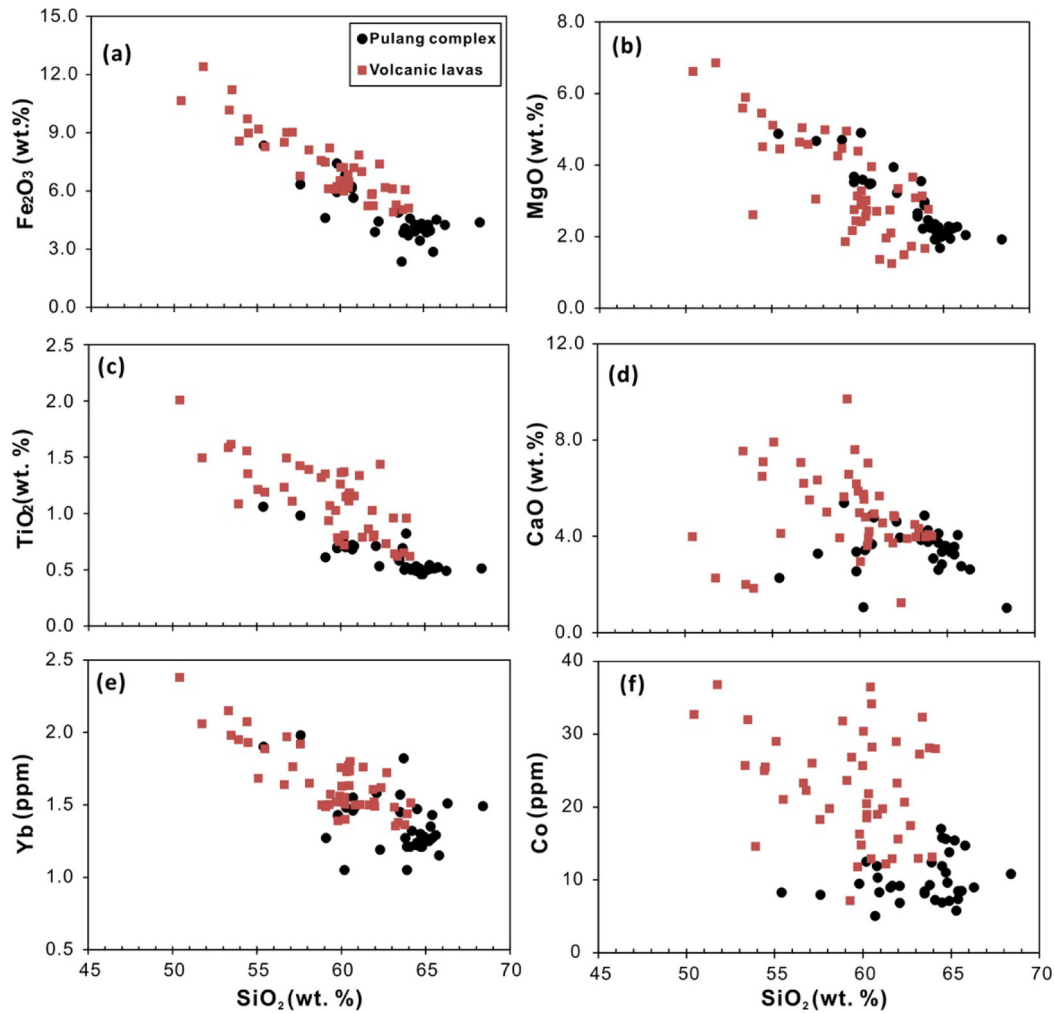
Fig. 10. Harker diagrams of selected major (a–d) and trace (e, f) elements for the Pulang complex (circle). Data of the volcanic wall rocks (square; Leng et al., 2014) are shown for comparison.

crystallization from a common parental magma (e.g., Sisson and Grove, 1993; Sisson et al., 2005; Feig et al., 2006; Ulmer, 2007), (2) mixing and hybridization of two end-member melts (e.g., Grove et al., 2005; Reubi and Blundy, 2009), and (3) the melt expulsion model (especially for rhyolite, Bachmann and Bergantz, 2004; Bachmann et al., 2007; Bachmann and Huber, 2016), in which the volcanic rocks are regarded as erupted melt-rich regions, while the crystal mush crystallized to form the plutons (mostly intermediate in composition). At Pulang, the extrusive rocks are more mafic than the intrusive rocks (Fig. 10), precluding the third model.

The Pulang complex is mainly andesitic to dacitic, broadly lying on the fractional crystallization trends defined by the lavas (Fig. 10a–f). This, however, does not support a co-magmatic origin, because no enrichments in incompatible elements were found in the volcanic rocks over the intrusive rocks, and both rock types are depleted in incompatible and compatible elements (Fig. 10e, f). In addition, the volcanic rocks have more positive $\varepsilon_{Hf}(t)$ (3.7 ± 0.3) and mantle-like $\delta^{18}O$ signatures (5.8‰) than those of the intrusive rocks ($\varepsilon_{Hf}(t) = -0.8–0.1$; $\delta^{18}O$ ratios <6.4‰), indicative of different origins. Thus, the whole-rock trace elements and zircon Hf-O isotopes do not support a common magmatic source between the intrusive and extrusive rocks at Pulang.

The consistent zircon Hf-O isotopes, together with the deficiency of inherited zircons in the Pulang complex (Fig. 4), suggest that crustal assimilation was likely minimal. Therefore, we propose that the parental magmas of the Pulang complex may have formed by mixing of two magmas, as supported by the wide variation range of

plagioclase phenocryst (An_6–An_{60}; Fig. 7) and amphibole (Fig. 9) compositions.

The covariant $\varepsilon_{Hf}(t)$ vs. $\delta^{18}O$ zircon arrays of the analyzed rocks exhibit a negative linear relationship (Fig. 13), implying a trend of magma mixing between two end-members (e.g., Kemp et al., 2007; Li et al., 2009). Our petrological modeling demonstrates that most zircons from the Pulang complex crystallized from a melt containing up to 40–50% crustal materials, and around 10–20% for the volcanic lavas (Fig. 13). On the other hand, the geometry (i.e., curvature) of the $\varepsilon_{Hf}(t)$ vs. $\delta^{18}O$ arrays can be used to constrain the relative Hf isotope compositions of the end-members (e.g., Kemp et al., 2007; Li et al., 2009). As shown in Fig. 13, the two end-members are expected to have similar Hf concentrations, which are substantiated by previous studies (He et al., 2013; Leng et al., 2014). Furthermore, the PGE variations in the studied rocks can also be explained by the mixing of two melt end-members. If the sample DSG11-15 (with the lowest SiO_2 and the highest PGE contents) is taken as the mafic end-member and the Upper Continental Crust (Rudnick and Gao, 2014) as the felsic end-member, most of the PGE data of the Pulang intrusive and extrusive rocks can be reproduced by mixing between the two end-members with various ratios (not shown).

To summarize, this study confirms that magma mixing is a plausible mechanism to produce the PGE variation observed at Pulang. A similar conclusion has also been reached in the study on the Kelian Au deposit (Setiabudi et al., 2007), implying that magma mixing may have been a common yet often underestimated phenomenon.
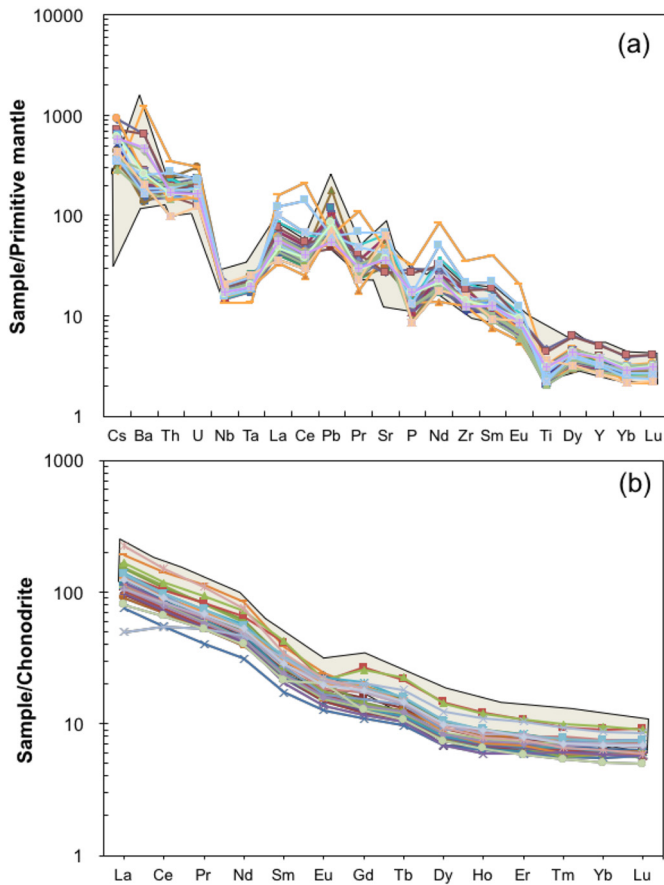
Fig. 11. Primitive mantle-normalized incompatible trace-element variation diagram (a), and chondrite-normalized REE diagram (b) for the Pulang complex. Primitive mantle and chondrite normalizing values are from Sun and McDonough (1989) and Boynton (1984), respectively.

5.3. Oxidized parental magma of the Pulang complex

As mentioned above, two types of amphibole, namely high-Al and low-Al amphiboles, were identified at the Pulang complex. Mineralogical compositions of different amphiboles can be used to evaluate the physicochemical conditions (e.g., pressure, temperature, oxygen fugacity and water content) of the parental magma from which the amphibole crystallized (Fig. 14), using the amphibole thermobarometers (e.g., Johnson and Rutherford, 1989; Ridolfi et al., 2010). The results show that the magmas equilibrated with the high-Al amphibole may have contained 4.8–6.2 wt% H_2O, and formed at a depth of 11–18 km at 858–935 °C, and an oxygen fugacity of NNO + 0.2–NNO + 1.5 (Fig. 14). Meanwhile, the melts equilibrated with the low-Al amphibole were likely more oxidized (NNO + 1.0–NNO + 1.7) but with lower H_2O content (4.2–4.9 wt%). They were likely formed at shallower depths (3–7 km) at low temperatures (770–810 °C). Although these two amphibole types contain different water contents (Fig. 14c), both were crystallized from oxidized magmas (>NNO + 0.2), as also supported by the large amount of magnetite observed. High fO_2 can significantly increase sulfur solubility in magmas (e.g., Jugo et al., 2005; Jugo, 2009; Hou and Zhang, 2015), and thus prohibit early sulfide saturation (e.g., Sun et al., 2015, 2017).

### 5.4. Removal and accumulation of sulfides during magma emplacement

Previous studies demonstrated that the PGE abundance in primary basaltic magmas are controlled largely by the degree of partial melting and the oxidization state of the mantle peridotite (Keays, 1995; Arndt et al., 2005; Naldrett, 2010; Gao et al., 2012, 2013). This is because PGE are extremely chalcophile, and are predominantly hosted by sulfide and/or alloy phases in the mantle. Therefore, either high-degree (>18–25%) of partial melting, or moderate-degree of melting (>11%) of an oxidized source (where sulfide phases are unstable), can significantly increase the PGE concentrations in the magmas (Arndt et al., 2005, and references therein).

In this study, the most mafic rocks (i.e., alkaline basalt) contain high PPGE concentrations (Pd = 5.9 ppb, Pt = 5.4 ppb), comparable to those

Table 3
Whole-rock PGE and Au concentrations (ppb) for the Pulang porphyries and volcanic wall rocks.

Sample	Lithology	Ir	Ru	Rh	Pt	Pd	Au	Pd/Pt	Pt/Ir
DSG07-8	TA	0.026	0.077	0.137	1.859	1.871	0.367	1.0	72
DSG10-1	TA	0.009	0.065	0.018	1.564	2.887	0.803	1.8	173
DSG10-7	TA	0.006	0.060	0.026	1.669	1.992	0.771	1.2	260
DSG10-15	AB	0.012	0.089	0.070	5.406	5.853	0.500	1.1	452
HN11-2	AB	0.019	0.102	0.010	1.177	1.160	0.844	1.0	62
HN11-5	AB	0.005	0.060	0.013	1.012	1.177	0.602	1.2	196
HN11-8	AB	0.005	0.056	0.004	1.204	1.964	0.415	1.6	248
PL12-16	AB	0.044	0.120	0.059	1.049	1.163	0.112	1.1	24
PL12-2	AP	0.058	0.107	0.181	4.676	3.855	0.297	0.8	81
PL12-1	AP	0.014	0.087	0.019	0.298	7.449	0.128	25.0	22
PLZKE004-373.4	QDP	0.020	0.072	0.030	2.371	2.128	4.451	0.9	119
PL12-23	QDP	0.017	0.090	0.061	1.918	1.892	0.086	1.0	116
PL12-9	QDP	0.027	0.095	0.070	2.749	3.409	2.068	1.2	103
PLZK5620-175	QDP	0.014	0.078	0.008	0.844	1.018	1.286	1.2	62
PLZK6628-504.8	MP	0.019	0.067	0.028	1.780	0.844	10.916	0.5	92
PLZK6628-273.5	MP	0.024	0.071	0.030	2.618	2.966	50.709	1.1	111
PLZKE004-135.3	GP	0.012	0.063	0.003	0.474	0.627	1.498	1.3	39
PLZK0416-835	GP	0.013	0.074	0.005	0.684	0.867	1.045	1.3	55
PL302-5	QMP	0.015	0.048	0.013	1.514	2.618	188.597	1.7	104
PLZK0406-132.2	QMP	0.008	0.067	0.000	0.351	0.729	2.799	2.1	47
PLZK0409-515	QMP	0.015	0.063	0.017	1.137	1.127	6.202	1.0	77
PLZK0406-297.5	QMP	0.019	0.079	0.011	0.998	0.869	13.927	0.9	53
PLZK0406-522	QMP	0.014	0.047	0.012	1.657	1.768	17.214	1.1	122
PLZK1208-872.7	QMP	0.104	0.046	0.022	1.593	2.073	16.079	1.3	15
PLZK1208-872.7 duplicate	QMP	0.017	0.048	0.013	1.289	3.455	17.919	2.7	77

Note: AB = alkaline basalt, other abbreviations of lithology are as in Table 1.
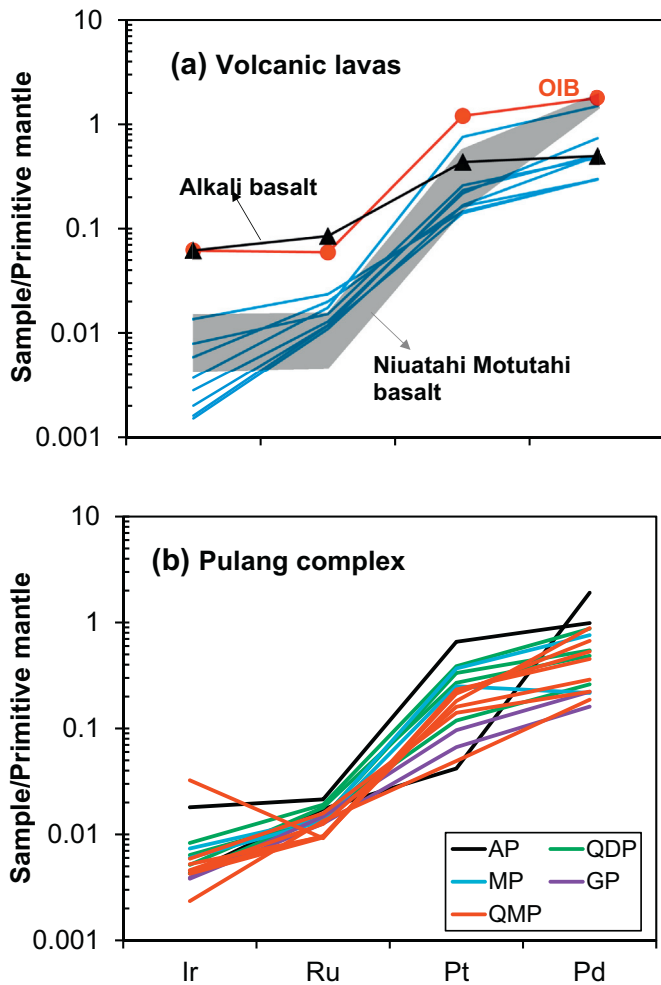
Fig. 12. Mantle-normalized plots of the volcanic lavas (a) and the Pulang complex (b). Primitive mantle normalizing values are from McDonough and Sun (1995). Data of the Niuatahi-Motutahi basalt (gray shade), OIB (circle), and alkaline basalt (triangle) are from Barnes and Lightfoot (2005), Park et al. (2015), and references therein. Abbreviation in b: AP = andesite porphyry; GP = granodiorite porphyry; QMP = quartz monzonite porphyry; MP = monzodiorite porphyry; QDP = quartz diorite porphyry.
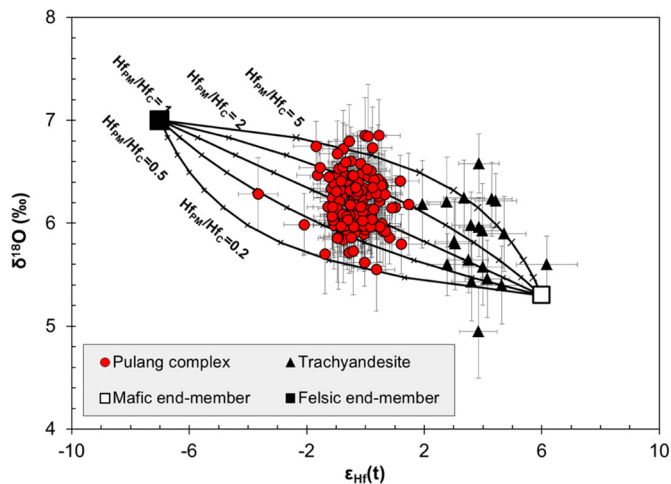
Fig. 13. Plot of zircon $\delta^{18}O$ vs. ε_{Hf} (t), showing the putative curves of magma mixing. Ticks on the curves represent 10% increments, and the ratio of Hf concentrations in the parental magma (PM) and crustal (C) end-ember (Hf$_{PM}$/Hf$_C$) is indicated for each. The $\delta^{18}O$ and ε_{Hf} (t) values are, respectively, assumed as 5.3‰ and +7 for the mafic end-member, and 7‰ and −7 for the felsic end-member, based on Valley et al. (2005); He et al. (2013); X.S. Wang et al. (2014a, b) and this study. See text for details.

of the typical arc basalts (e.g., basalts from the Tonga Rear Arc; Park et al., 2015), and higher than those of basalts from the Cameroon Line suite, which were suggested to have formed from low-degree (<8%) partial melting of mantle peridotite (Rehkämper et al., 1999). The oxidized nature of the parental magmas at Pulang indicates that sulfides may not have saturated during the magma emplacement, so that the PGE contents in the silicate melts remain unchanged. Due to the higher partition coefficients between the sulfide and silicate melts of Pt against Pd (Fleet et al., 1999), sulfide crystallization would increase the Pd/Pt ratios in the residual magmas (>1). At Pulang, most of the volcanic rocks have consistent Pd/Pt ratios of ~1 (Fig. 12; Table 3), indicating that the lavas may not have fractionated Pt-alloys or sulfides. Therefore, IPGE-depleted signatures of the Pulang intrusive and extrusive rocks suggest that the parental magmas may have formed by low-degree (<11%) partial melting of a PGE-depleted mantle source. Nonetheless, the IPGE depletions could also be led by the presence of certain IPGE-rich phases (e.g., alloy, Cr spinel and chromite; Barnes and Lightfoot, 2005) in the melt residue.

We propose that the Pulang magma did not undergo early sulfide removal, and that the magma was likely sulfide-unsaturated during its emplacement. Although the Pulang intrusive complex and the volcanic wall rocks contain slightly varying PGE concentrations (Table 3), all the rocks do not show PGE enrichments relative to OIB (Fig. 12). The sulfide-unsaturated magma would dissolve sulfides, if any, in the crust and elevate its PGE contents due to extremely high PGE budget in such sulfides. Thus, the relatively low PGE contents of the Pulang magmatic rocks preclude the existence of early Cu-rich sulfide accumulation at depth.

5.5. Ore-forming controls of the Pulang Cu-Au deposit

This study concludes that both the intrusive and extrusive rocks at Pulang have not experienced early sulfide removal or addition, and thus the parental magmas were likely sulfide-unsaturated prior to their emplacement. Although these magmas were oxidized, which is favorable for ore metal transport, they may have different physicochemical properties as indicated by the varying amphibole compositions (Fig. 14). Volatile (mainly water) contents were likely increased in the residual melts via magmatic differentiation and/or via mafic magma replenishments. Furthermore, as reflected by the low-Al amphibole compositions (Fig. 14), the inferred H$_2$O$_{melt}$ content decreases (<4.9 wt%) with increasing oxygen fugacity (>NNO + 1.0). This may have occurred during the onset of volatile exsolution at shallow depths, and represents another factor that promoted ore formation (Cline, 2003). High water contents promote the exsolution of aqueous fluids (e.g., Richards, 2011; R. Wang et al., 2014), and substantially increase the efficiency of metal extraction from the silicate melts (or crystal mush). Thus, both high oxygen fugacity and water contents are critical ore-forming factors for the Pulang porphyry Cu-Au deposit.

6. Conclusions

Both the Pulang complex and the mafic-intermediate volcanic wall rocks have similar PGE abundances and mantle-normalized PGE patterns, implying that no appreciable sulfide cumulates were lost or gained during the magma fractionation in the upper crust.

The Pulang complex was likely formed in a long-lived (~5 m.y.) open magmatic system, and has experienced complex processes of magma mixing and replenishment.

Two kinds of amphibole with different Al$_2$O$_3$ contents are identified at Pulang, which were likely crystallized in the deeper (11–18 km) and shallower (3–7 km) parts of the magma chambers, respectively.

High oxygen fugacity and high water contents were two critical ore-forming factors for the Pulang porphyry Cu-Au deposit.
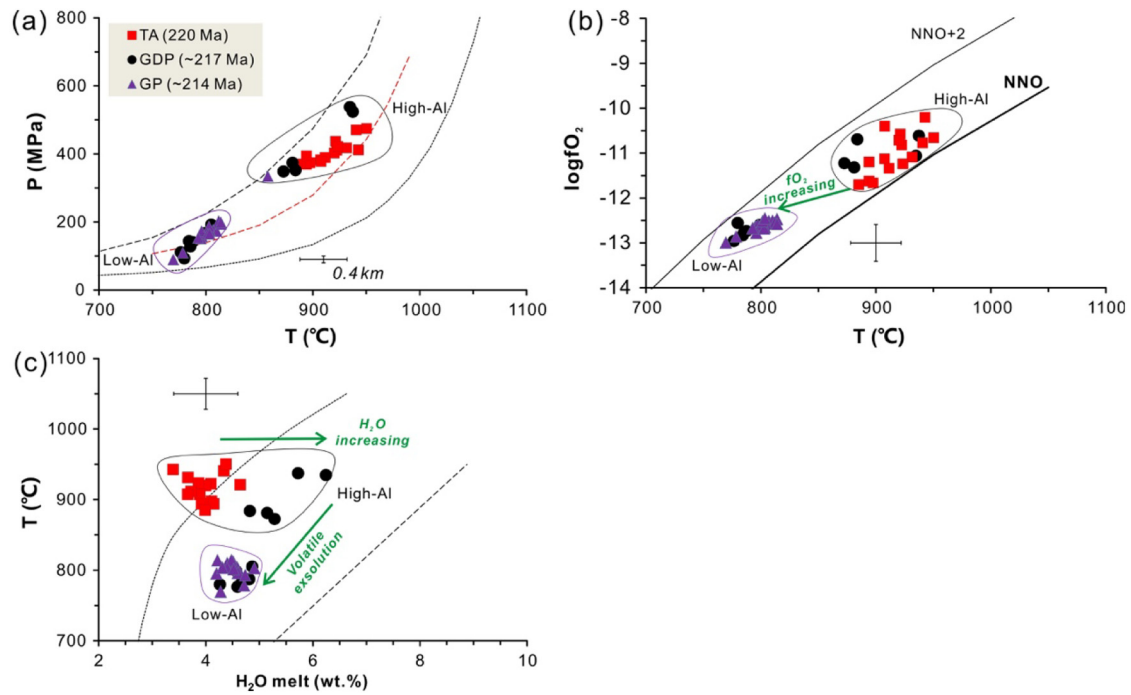
Fig. 14. Plots of pressure (a), log f_{O_2} (b) and H_2O_{melt} (c) versus temperature estimated from the Pulang amphiboles. All the diagrams were from the spreadsheet of Ridolfi et al. (2010). The pressure was calculated based on the Al-in-hornblende barometer of Johnson and Rutherford (1989). Error bars represent the expected rest (22 °C) and maximum log f_{O_2} errors (0.4 log unit). Abbreviations: NNO = nickel nickel oxide buffer curve (O'Neill and Pownceby, 1993), others are the same as in Fig. 12.

Acknowledgments

Appendix A. Supplementary data

Supplementary data to this article can be found online at https://doi.org/10.1016/j.gr.2018.03.001.

References

Arndt, N., Lesher, C., Czamanske, G., 2005. Mantle-derived magmas and magmatic Ni-Cu-(PGE) deposits. Economic Geology 100th Anniversary. vol. 34, pp. 5–24.

Bachmann, O., Bergantz, G.W., 2004. On the origin of crystal-poor rhyolites: extracted from batholithic crystal mushes. Journal of Petrology 45 (8), 1565–1582.

Bachmann, O., Huber, C., 2016. Silicic magma reservoirs in the Earth's crust. American Mineralogist 101, 2377–2404.

Bachmann, O., Miller, C.F., Silva, S.L.D., 2007. The volcanic–plutonic connection as a stage for understanding crustal magmatism. Journal of Volcanology and Geothermal Research 167, 1–23.

Baker, J., Peate, D., Waight, T., Meyzen, C., 2004. Pb isotopic analysis of standards and samples using a ^{207}Pb–^{204}Pb double spike and thallium to correct for mass bias with a double-focusing MC-ICP-MS. Chemical Geology 211 (3–4), 275–303.

Barnes, S.J., Lightfoot, P.C., 2005. Formation of magmatic sulfide ore deposits and processes affecting their copper and platinum group element contents. Econ Geol 100th Anniversary. vol. 34, pp. 179–214.

Black, L.P., Kamo, S.L., Allen, C.M., Aleinikoff, J.N., Davis, D.W., Korsch, R.J., Foudoulis, C., 2003. TEMORA 1: a new zircon standard for Phanerozoic U–Pb geochronology. Chemical Geology 200 (1–2), 155–170.

Botcharnikov, R.E., Linnen, R.L., Wilke, M., Holtz, F., Jugo, P.J., Berndt, J., 2011. High gold concentrations in sulphide-bearing magma under oxidizing conditions. Nature Geoscience 4, 112–115.

Botcharnikov, R.E., Holtz, F., Mungall, J.E., Beermann, O., Linnen, R.L., Garbe-Schönberg, Dieter, 2013. Behavior of gold in a magma at sulfide-sulfate transition: revisited. American Mineralogist 98 (8–9), 1459–1464.

Boynton, W.V., 1984. Geochemistry of the rare earth elements: meteorite studies. In: Henderson, P. (Ed.), Rare Earth Element Geochemistry. Elsevier, pp. 63–114.

Chen, J.L., Xu, J.F., Ren, J.B., Huang, X.X., Wang, B.D., 2014. Geochronology and geochemical characteristics of Late Triassic porphyritic rocks from the Zhongdian arc, eastern Tibet, and their tectonic and metallogenic implications. Gondwana Research 26 (2), 492–504.

Chiaradia, M., 2013. Copper enrichment in arc magmas controlled by overriding plate thickness. Nature Geoscience 7, 43–46.

Cline, J.S., 2003. How to concentrate copper. Science 302, 2075–2076.

Cocker, H.A., Valente, D.L., Park, J.W., Campbell, I.H., 2016. Using platinum group elements to identify sulfide saturation in a porphyry Cu system: the El Abra porphyry Cu deposit, Northern Chile. Journal of Petrology 56 (12), 2491–2514.

Cooke, D.R., Hollings, P., Walshe, J.L., 2005. Giant porphyry deposits: characteristics, distribution, and tectonic controls. Economic Geology 100 (5), 801–818.

Deng, J., Wang, Q.F., Li, G.J., Li, C., Wang, C.M., 2014. Tethys tectonic evolution and its bearing on the distribution of important mineral deposits in the Sanjiang region, SW China. Gondwana Research 26 (2), 419–437.

Deng, J., Wang, Q.F., Li, G.J., 2017. Tectonic evolution, superimposed orogeny, and composite metallogenic system in China. Gondwana Research 50, 216–266.

Economou-Eliopoulos, M., Eliopoulos, D.G., 2000. Palladium, platinum and gold concentration in porphyry copper systems of Greece and their genetic significance. Ore Geology Reviews 16, 59–70.

Feig, S.T., Koepke, J., Snow, J.E., 2006. Effect of water on tholeiitic basalt phase equilibria: an experimental study under oxidizing conditions. Contributions to Mineralogy and Petrology 152, 611–638.

Fleet, M.E., Crocket, J.H., Liu, M.H., Stone, W.E., 1999. Laboratory partitioning of platinum-group elements (PGE) and gold with application to magmatic sulfide-PGE deposits. Lithos 47 (1), 127–142.

Gao, J.F., Zhou, M.F., Lightfoot, P.C., Wang, C.Y., Qi, L., 2012. Origin of PGE-poor and Cu-rich magmatic sulfides from the Kalatongke deposit, Xinjiang, Northwest China. Economic Geology 107 (3), 481–506.

Gao, J.F., Zhou, M.F., Lightfoot, P.C., Wang, C.Y., Qi, L., Sun, M., 2013. Sulfide-saturation and magma emplacement in the formation of the Permian Huangshandong Ni-Cu sulfide deposit, Xinjiang, NW China. Economic Geology 108, 1833–1848.

Gao, J.F., Zhou, M.F., Qi, L., Chen, W.T., Huang, X.W., 2015. Chalcophile elemental compositions and origin of the Tuwu porphyry Cu deposit, NW China. Ore Geology Reviews 66, 403–421.

Grove, T.L., Baker, M.B., Price, R.C., Parman, S.W., Elkins-Tanton, L.T., Chatterjee, N., Müntener, O., 2005. Magnesian andesite and dacite lavas from Mt. Shasta, northern California: products of fractional crystallization of H₂O-rich mantle melts. Contributions to Mineralogy and Petrology 148 (5), 542–565.

Hao, H., Campbell, I.H., Park, J.-W., Cooke, D.R., 2017. Platinum-group element geochemistry used to determine Cu and Au fertility in the Northparkes igneous suites, New South Wales, Australia. Geochimica et Cosmochimica Acta 216, 372–392.

He, D.F., Zhu, W.G., Zhong, H., Ren, T., Bai, Z.J., Fan, H.P., 2013. Zircon U–Pb geochronology and elemental and Sr–Nd–Hf isotopic geochemistry of the Daocheng granitic pluton from the Yidun Arc, SW China. Journal of Asian Earth Sciences 67–68, 1–17.

Hou, Z.Q., Zhang, H.R., 2015. Geodynamics and metallogeny of the eastern Tethyan metallogenic domain. Ore Geology Reviews 70, 346–384.

Hou, Z.Q., Zaw, K., Pan, G.T., Mo, X.X., Xu, Q., Hu, Y.Z., Li, X.Z., 2007. Sanjiang Tethyan metallogenesis in S.W. China: tectonic setting, metallogenic epochs and deposit types. Ore Geology Reviews 31, 48–87.

Hou, Z.Q., Zhou, Y., Wang, R., Zheng, Y.C., He, W.Y., Zhao, M., Evans, N.J., Weinberg, R.F., 2017. Recycling of metal-fertilized lower continental crust: origin of non-arc Au-rich porphyry deposits at cratonic edges. Geology 45, 563–566.

Hu, Z.C., Liu, Y.S., Gao, S., Xiao, L.S., Günther, D., Li, M., Zhang, W., Zong, K.Q., 2012. A "wire" signal smoothing device for laser ablation inductively coupled plasma mass spectrometry analysis. Spectrochimica Acta Part B: Atomic Spectroscopy 78, 50–57.

Jackson, S.E., Pearson, N.J., Griffin, W.L., Belousova, E.A., 2004. The application of laser ablation-inductively coupled plasma-mass spectrometry to in situ U–Pb zircon geochronology. Chemical Geology 211 (1–2), 47–69.

Johnson, M.C., Rutherford, M.J., 1989. Experimental calibration of the aluminum- in-hornblende geobarometer with application to Long Valley caldera (California) volcanic rocks. Geology 17 (9), 837–841.

Jugo, P.J., 2009. Sulfur content at sulfide saturation in oxidized magmas. Geology 37 (5), 415–418.

Jugo, P.J., Luth, R.W., Richards, J.P., 2005. Experimental data on the speciation of sulfur as a function of oxygen fugacity in basaltic melts. Geochimica et Cosmochimica Acta 69 (2), 497–503.

Keays, R.R., 1995. The role of komatiitic and picritic magmatism and S-saturation in the formation of ore deposits. Lithos 34 (1), 1–18.

Kemp, A.I.S., Hawkesworth, C.J., Foster, G.L., Paterson, B.A., Woodhead, J.D., Hergt, J.M., Gray, C.M., Whitehouse, M.J., 2007. Magmatic and crustal differentiation history of granitic rocks from Hf-O isotopes in zircon. Science 315, 980–983.

Leake, B.E., Woolley, A.R., Arps, C.E., Birch, W.D., Gilbert, M.C., Grice, J.D., Hawthorne, F.C., Kato, A., Kisch, H.J., Krivovichev, V.G., 1997. Nomenclature of amphiboles: report of the subcommittee on amphiboles of the International Mineralogical Association Commission on New Minerals and Mineral Names. Mineralogical Magazine 61 (405), 295–321.

Lee, C.-T.A., Luffi, P., Chin, E.J., Bouchet, R., Dasgupta, R., Morton, D.M., Le Roux, V., Yin, Q.Z., Jin, D., 2012. Copper systematics in arc magmas and implications for crust-mantle differentiation. Science 336, 64–68.

Leng, C.B., Zhang, X.C., Hu, R.Z., Wang, S.X., Zhong, H., Wang, W.Q., Bi, X.W., 2012. Zircon U-Pb and molybdenite Re-Os geochronology and Sr-Nd-Pb-Hf isotopic constraints on the genesis of the Xuejiping porphyry copper deposit in Zhongdian, Northwest Yunnan, China. Journal of Asian Earth Sciences 60, 31–48.

Leng, C.B., Huang, Q.Y., Zhang, X.C., Wang, S.X., Zhong, H., Hu, R.Z., Bi, X.W., Zhu, J.J., Wang, X.S., 2014. Petrogenesis of the Late Triassic volcanic rocks in the Southern Yidun arc, SW China: constraints from the geochronology, geochemistry, and Sr–Nd–Pb–Hf isotopes. Lithos 190–191, 363–382.

Li, X.H., Li, W.X., Wang, X.C., Li, Q.L., Yu, L., Tang, G.Q., 2009. Role of mantle-derived magma in genesis of early Yanshanian granites in the Nanling Range, South China: in situ zircon Hf-O isotopic constraints. Science China Earth Sciences 52 (9), 1262–1278.

Li, X.H., Long, W.G., Li, Q.L., Liu, Y., Zheng, Y.F., Yang, Y.H., Chamberlain, K.R., Wan, D.F., Guo, C.H., Wang, X.C., 2010. Penglai zircon megacrysts: a potential new working peference material for microbeam determination of Hf–O isotopes and U–Pb age. Geostandards and Geoanalytical Research 34, 117–134.

Li, W.C., Zeng, P.S., Hou, Z.Q., White, N.C., 2011. The Pulang porphyry copper deposit and associated felsic intrusions in Yunnan Province, southwest China. Economic Geology 106 (1), 79–92.

Li, X.H., Tang, G.Q., Guo, B., Yang, Y.H., Hou, K.J., Hu, Z.C., Li, Q.L., Liu, Y., Li, W.X., 2013. Qinghu zircon: a working reference for microbeam analysis of U-Pb age and Hf and O isotopes. Science Bulletin 58, 4647–4654.

Liu, Y., Gao, S., Hu, Z., Gao, C., Zong, K., Wang, D., 2010. Continental and oceanic crust recycling-induced melt–peridotite interactions in the Trans-North China Orogen: U–Pb dating, Hf isotopes and trace elements in zircons from mantle xenoliths. Journal of Petrology 51, 537–571.

Ludwig, K.R., 2003. User's Manual for Isoplot 3.75, a Geochronological Toolkit for Microsoft Excel. Berkeley Geochronology Center Special Publication, Berkeley, CA, USA (75 pp., no. 5).

McDonough, W.F., Sun, S.S., 1995. The composition of the Earth. Chemical Geology 120 (3–4), 223–253.

Meffre, S., Large, R.R., Scott, R., Woodhead, J., Chang, Z.S., Gilbert, S.E., Danyushevsky, L.V., Maslennikov, V., Hergt, J.M., 2008. Age and pyrite Pb-isotopic composition of the giant Sukhoi Log sediment-hosted gold deposit, Russia. Geochimica et Cosmochimica Acta 72 (9), 2377–2391.

Mungall, J.E., Brenan, J.M., 2014. Partitioning of platinum-group elements and Au between sulfide liquid and basalt and the origins of mantle-crust fractionation of the chalcophile elements. Geochimica et Cosmochimica Acta 125, 265–289.

Naldrett, A.J., 2010. From the mantle to the bank: the life of a Ni-Cu-(PGE) sulfide deposit. South African Journal of Geology 113 (1), 1–32.

O'Neill, H.S., Pownceby, M.I., 1993. Thermodynamic data from redox reactions at high temperatures. I. An experimental and theoretical assessment of the electrochemical method using stabilized zirconia electrolytes, with revised values for the Fe-"FeO", Co-CoO, Ni-NiO, and Cu-Cu₂O oxygen buffers, and new data for the W-WO₂ buffer. Contributions to Mineralogy and Petrology 114, 296–314.

Pang, Z.S., Du, Y.S., Wang, G.W., Guo, X., Cao, Y., Li, Q., 2009. Single-grain zircon U-Pb isotopic ages, geochemistry and its implication of the Pulang complex in Yunnan Province, China. Acta Petrologica Sinica 25 (1), 159–165 (in Chinese with English abstract).

Park, J.W., Campbell, I.H., Kim, J., Moon, J.W., 2015. The role of late sulfide saturation in the formation of a Cu- and Au-rich magma: insights from the platinum group element geochemistry of Niuatahi–Motutahi lavas, Tonga rear arc. Journal of Petrology 56 (1), 59–81.

Qi, L., Hu, J., Gregoire, D.C., 2000. Determination of trace elements in granites by inductively coupled plasma mass spectrometry. Talanta 51 (3), 507–513.

Qi, L., Zhou, M.F., Wang, C.Y., 2004. Determination of low concentrations of platinum group elements in geological samples by ID-ICP-MS. Journal of Analytical Atomic Spectrometry 19, 1335–1339.

Qi, L., Zhou, M.F., Yan, W.C., Sun, M., 2007. Evaluation of a technique for determining Re and PGEs in geological samples by ICP-MS coupled with a modified Carius tube design. Geochemical Journal 41, 407–414.

Qi, L., Zhou, M.F., Gao, J.F., Zhao, Z., 2010. An improved Carius tube technique for determination of low concentrations of Re and Os in pyrites. Journal of Analytical Atomic Spectrometry 25, 585–589.

Qu, X.M., Hou, Z.Q., Zhou, S.G., 2002. Geochemical and Nd, Sr isotopic study of the post-orogenic granites in the Yidun arc belt of northern Sanjiang region, southwestern China. Resource Geology 52, 163–172.

Rehkämper, M., Halliday, A.N., Fitton, J.G., Lee, D.C., Wieneke, M., Arndt, N.T., 1999. Ir, Ru, Pt, and Pd in basalts and komatiites: new constraints for the geochemical behavior of the platinum-group elements in the mantle. Geochimica et Cosmochimica Acta 63, 3915–3934.

Reid, A.J., Wilson, C.J.L., Phillips, D., Liu, S., 2005. Mesozoic cooling across the Yidun Arc, central-eastern Tibetan Plateau: a reconnaissance ⁴⁰Ar/³⁹Ar study. Tectonophysics 398 (1–2), 45–66.

Reubi, O., Blundy, J., 2009. A dearth of intermediate melts at subduction zone volcanoes and the petrogenesis of arc andesites. Nature 461, 1269–1273.

Richards, J.P., 2003. Tectono-magmatic precursors for porphyry Cu-(Mo-Au) deposit formation. Economic Geology 98 (8), 1515–1533.

Richards, J.P., 2011. Magmatic to hydrothermal metal fluxes in convergent and collided margins. Ore Geology Reviews 40 (1), 1–26.

Richards, J.P., 2015. The oxidation state, and sulfur and Cu contents of arc magmas: implications for metallogeny. Lithos 233, 27–45.

Ridolfi, F., Renzulli, A., Puerini, M., 2010. Stability and chemical equilibrium of amphibole in calc-alkaline magmas: an overview, new thermobarometric formulations and application to subduction-related volcanoes. Contributions to Mineralogy and Petrology 160 (1), 45–66.

Rudnick, R., Gao, S., 2014. Composition of the continental crust. In: Holland, H.D., Turekian, K.K. (Eds.), Treatise on Geochemistry, 2nd ed. vol. 4. Elsevier, Oxford, pp. 1–51.

Sack, P.J., Berry, R.F., Sebastien, M., Falloon, T.J., Bruce, G.J., Friedman, R.M., 2011. In situ location and U-Pb dating of small zircon grains in igneous rocks using laser ablation–inductively coupled plasma–quadrupole mass spectrometry. Geochemistry, Geophysics, Geosystems 12, 99–108.

Setiabudi, B.T., Campbell, I.H., Martin, C.E., Allen, C.M., 2007. Platinum group element geochemistry of andesite intrusions of the Kelian region, East Kalimantan, Indonesia: implications of gold depletion in the intrusions associated with the Kelian gold deposit. Economic Geology 102 (1), 95–108.

Sillitoe, R.H., 1972. A plate tectonic model for the origin of porphyry copper deposits. Economic Geology 67 (2), 184–197.

Sillitoe, R.H., 1973. The tops and bottoms of porphyry copper deposits. Economic Geology 68 (6), 799–815.

Sillitoe, R.H., 1998. Major regional factors favouring large size, high hypogene grade, elevated gold content and supergene oxidation and enrichment ofs porphyry copper deposits. In: Porter, T.M. (Ed.), Porphyry and Hydrothermal Copper and Gold Deposits: A Global Perspective. Australian Mineral Foundation, Adelaide, pp. 21–34.

Sillitoe, R.H., 2010. Porphyry copper systems. Economic Geology 105 (1), 3–41.

Sillitoe, 2012. Copper provinces. Society of Economic Geologists, Inc., Special Publication, 16, pp. 1–18.

Sisson, T.W., Grove, T.L., 1993. Experimental investigations of the role of H₂O in calc-alkaline differentiation and subduction zone magmatism. Contributions to Mineralogy and Petrology 113, 143–166.

Sisson, T.W., Ratajeski, K., Hankins, W.B., Glazner, A.F., 2005. Voluminous granitic magmas from common basaltic sources. Contributions to Mineralogy and Petrology 148, 635–661.

Sun, S.S., McDonough, W.F., 1989. Chemical and isotopic systematics of oceanic basalts: implications for mantle composition and processes. In: Saunders, A.D., Norry, M.J. (Eds.), Magmatism in the Ocean Basins. Geological Society London Special Publications 42, pp. 313–345.

Sun, W.D., Huang, R.F., Li, H., Hu, Y.B., Zhang, C.C., Sun, S.J., Zhang, L.P., Ding, X., Li, C.Y., Zartman, R.E., Ling, M.X., 2015. Porphyry deposits and oxidized magmas. Ore Geology Reviews 65, 97–131.

Sun, W.D., Wang, J.T., Zhang, L.P., Zhang, C.C., Li, H., Ling, M.X., Ding, X., Li, C.Y., Liang, H.Y., 2017. The formation of porphyry copper deposits. Acta Geochimica 36 (1), 9–15.

Tatsumi, Y., Hamilton, D.L., Nesbitt, R.W., 1986. Chemical characteristics of fluid phase released from a subducted lithosphere and origin of arc magmas: evidence from high-pressure experiments and natural rocks. Journal of Volcanology and Geothermal Research 29 (1–4), 293–309.

Tindle, A., Webb, P., 1994. PROBE-AMPH—a spreadsheet program to classify microprobe-derived amphibole analyses. Computers and Geosciences 20 (7–8), 1201–1228.

Tosdal, R.M., Dilles, J.H., Cooke, D.R., 2009. From source to sinks in auriferous magmatic-hydrothermal porphyry and epithermal deposits. Elements 5 (5), 289–295.

Ulmer, P., 2007. Differentiation of mantle-derived calc-alkaline magmas at mid to lower crustal levels: experimental and petrologic constraints. Periodico di Mineralogia 76 (3), 309–325.

Valley, J.W., Lackey, J.S., Cavosie, A.J., Clechenko, C.C., Spicuzza, M.J., Basei, M.A.S., Bindeman, I.N., Ferreira, V.P., Sial, A.N., King, E.M., Peck, W.H., Sinha, A.K., Wei, C.S., 2005. 4.4 billion years of crustal maturation: oxygen isotope ratios of magmatic zircon. Contributions to Mineralogy and Petrology 150, 561–580.

Wang, S.X., 2008. Ore Geochemistry of the Pulang Porphyry Copper Deposit, Yunnan Province, China. Institute of Geochemistry. University of Chinese Academy of Sciences, Guiyang, p. 134 (in Chinese with English abstract).

Wang, B.Q., Zhou, M.F., Li, J.W., Yan, D.P., 2011. Late Triassic porphyritic intrusions and associated volcanic rocks from the Shangri-La region, Yidun terrane, Eastern Tibetan Plateau: Adakitic magmatism and porphyry copper mineralization. Lithos 127 (1–2), 24–38.

Wang, R., Richards, J.P., Hou, Z., Yang, Z., DuFrane, S.A., 2014. Increased magmatic water content—the key to Oligo-Miocene porphyry Cu-Mo ± Au formation in the Eastern Gangdese Belt, Tibet. Economic Geology 109 (7), 1315–1339.

Wang, X.S., Bi, X.W., Leng, C.B., Zhong, H., Tang, H.F., Chen, Y.W., Yin, G.H., Huang, D.Z., Zhou, M.-F., 2014a. Geochronology and geochemistry of Late Cretaceous igneous intrusions and Mo–Cu–(W) mineralization in the southern Yidun Arc, SW China: implications for metallogenesis and geodynamic setting. Ore Geology Reviews 61, 73–95.

Wang, X.S., Hu, R.Z., Bi, X.W., Leng, C.B., Pan, L.C., Zhu, J.J., Chen, Y.W., 2014b. Petrogenesis of Late Cretaceous I-type granites in the southern Yidun Terrane: new constraints on the Late Mesozoic tectonic evolution of the eastern Tibetan Plateau. Lithos 208–209, 202–219.

Watson, E.B., Wark, D.A., Thomas, J.B., 2006. Crystallization thermometers for zircon and rutile. Contributions to Mineralogy and Petrology 151, 413–433.

Wiedenbeck, M., Alle, P., Corfu, F., Griffin, W.L, Meier, M., Oberli, F., Vonquadt, A., Roddick, J.C., Speigel, W., 1995. Three natural zircon standards for U-Th-Pb, Lu-Hf, trace element and REE analyses. Geostandards Newsletter 19 (1), 1–23.

Zeng, P.S., Li, W.C., Wang, H.P., Li, H., 2006. The Indosinian Pulang superlarge porphyry copper deposit in Yunnan, China: petrology and chronology. Acta Petrologica Sinica 22 (4), 989–1000 (in Chinese with English abstract).